

## Continued glacial retreat linked to changing macronutrient supply along the West Antarctic Peninsula

Rhiannon L. Jones<sup>a,\*</sup>, Michael P. Meredith<sup>b</sup>, Maeve C. Lohan<sup>a</sup>, E. Malcolm S. Woodward<sup>c</sup>, Katrien Van Landeghem<sup>d</sup>, Kate Retallick<sup>d</sup>, Oliver Flanagan<sup>a</sup>, Mehul Vora<sup>e</sup>, Amber L. Annett<sup>a</sup>

<sup>a</sup> School of Ocean and Earth Science, University of Southampton, National Oceanography Centre, European Way, Southampton SO14 3ZH, UK

<sup>b</sup> British Antarctic Survey, Cambridge CB3 0ET, UK

<sup>c</sup> Plymouth Marine Laboratory, Plymouth PL1 3DH, UK

<sup>d</sup> Bangor University, Bangor LL57 2DG, UK

<sup>e</sup> Rutgers University, NJ, USA

### ARTICLE INFO

#### Keywords:

Radium  
Macronutrient cycling  
Glacial retreat  
West Antarctic Peninsula

### ABSTRACT

At the West Antarctic Peninsula (WAP), continued atmospheric and oceanic warming is causing significant physical and biogeochemical changes to glaciers and the marine environment. We compare sediment sources and drivers of macronutrient distributions at two bays along the WAP during austral summer 2020, using radioactive radium and stable oxygen isotopes to trace sedimentary influences and quantify different freshwater inputs. In the Ryder Bay, where the Sheldon Glacier is marine-terminating, radium activities at the sediment-water interface indicate considerable benthic mixing. Using radium isotope activity gradients to resolve radium and macronutrient fluxes, we find buoyant meltwater proximal to the glacier drives vigorous mixing of sediment and entrainment of macronutrient deep waters, on the order of  $2.0 \times 10^5 \text{ mol d}^{-1}$  for nitrate. Conversely, in the Marian Cove, where the Fourcade Glacier terminates on land, low salinities and oxygen isotopes indicate a meltwater-rich surface layer <1 m thick and rich in sediment, and strong vertical mixing to the seafloor. A continued shift to land-terminating glaciers along the WAP may have a significant impact upon nutrient and sediment supply to the euphotic zone, with impacts upon primary productivity and carbon uptake efficiency. The future of primary production, carbon uptake, and food web dynamics is therefore linked to glacier retreat dynamics in the many fjords along the WAP.

### 1. Introduction

Since the middle of the last century, marked atmospheric and ocean warming along the West Antarctic Peninsula (WAP) has led to the rapid retreat of glaciers, retreat of sea ice and shortening of the sea ice season (Turner et al., 2015; Massom et al., 2018; Stammerjohn et al., 2015; Cook et al., 2016). The retreat of marine-terminating glaciers in the central and southern WAP is driven predominantly by the incursion of upper Circumpolar Deep Water (CDW) from the deep layers of the Antarctic Circumpolar Current onto the WAP shelf. This water has warmed by 0.1–0.3 °C decade<sup>-1</sup> since the 1990s (Schmidtko et al., 2014), enhancing melt rates at the glacier-water column interface (Cook et al., 2016). Incursions of CDW onto the shelf undergo modification through mixing associated with topographic overflows (Venables et al., 2017). This modified CDW (mCDW) provides the dominant source of

macronutrients to the coastal WAP (Henley et al., 2018; Henley et al., 2017; Dierssen et al., 2002). Primary inputs from sea ice melt, terrigenous sources and glacial melt are comparatively small (Pedulli et al., 2014).

At the northern tip of the WAP, the deep ocean waters of the Bransfield Strait are colder than the mCDW further south, influenced by cold Weddell Sea waters from the east (Cook et al., 2016). The primary control on glacial retreat in the Bransfield Strait region appears to be atmospheric and surface processes: westerly winds drive warm and moist air across the northern WAP, thinning the coastal ice shelves and increasing meltwater discharge from surface runoff and ablation (Rignot et al., 2004).

Meltwater inputs to surface waters lower the salinity of the upper water column, and typically strengthen stratification. Studies along the WAP have focussed on sea-ice dynamics, however water column

\* Corresponding author.

E-mail address: [r.l.c.jones@soton.ac.uk](mailto:r.l.c.jones@soton.ac.uk) (R.L. Jones).

<https://doi.org/10.1016/j.marchem.2023.104230>

Received 13 July 2022; Received in revised form 15 February 2023; Accepted 20 February 2023

Available online 27 February 2023

0304-4203/© 2023 The Authors. Published by Elsevier B.V. This is an open access article under the CC BY license (<http://creativecommons.org/licenses/by/4.0/>).

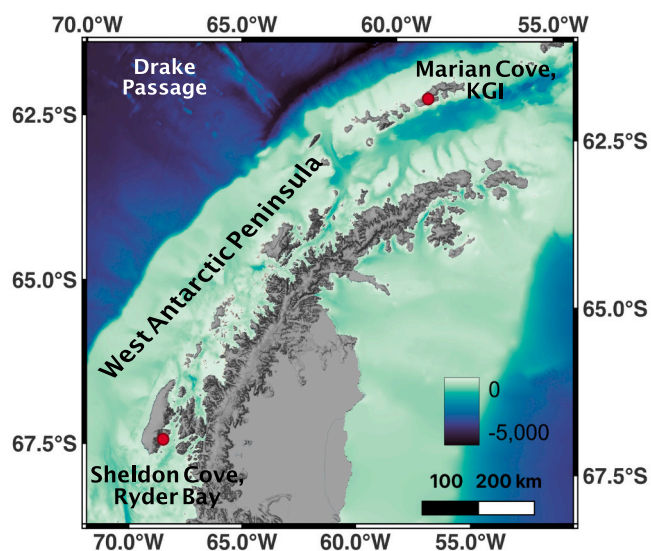


Fig. 1. Regional map of the West Antarctic Peninsula, with the two main study sites and located by red dots. Bathymetry data is from the ETOPO 2022 global relief model (<https://doi.org/10.25921/fd45-gt74>). Map was created using QGIS. (For interpretation of the references to colour in this figure legend, the reader is referred to the web version of this article.)

changes due to glacial melt have varying impacts upon primary production, such as providing favourable growing conditions through a shallow mixed layer (Pan et al., 2020), initiating a spring bloom (Dierssen et al., 2002), or changing the phytoplankton community composition (Moline et al., 2004). Both surface runoff and subglacial meltwater via deep channels can carry a significant lithogenic load. Through physical and chemical erosion of underlying bedrock material, meltwater may be enriched in nitrate and phosphate (Hodson et al., 2005), bioavailable micronutrients such as nanoparticulate iron (oxy)hydroxides (Lippiatt et al., 2010; Hawkings et al., 2018; Hodson et al., 2017) and dissolved silicic acid (Brown et al., 2010; Meire et al., 2016), the supply of which can alleviate nutrient limitation and increase primary production (Gerringa et al., 2012; Meire et al., 2016). Meltwater inputs at the grounding line of marine-terminating glaciers can drive upward fluxes of macro- and micronutrients such as silicic acid (Ng et al., 2020) and iron (Halbach et al., 2019) through shelf sediment resuspension. Arctic studies show that buoyant meltwater can entrain nutrient-rich waters upwards as it rises, supplying the euphotic zone and potentially alleviating nutrient limitation (Cape et al., 2019a; Kanna et al., 2018; Meire et al., 2017). Given the rapid climatic changes at the WAP and the projections for these to continue, there is a need to understand better the role of glacial meltwater in nutrient cycling, and how it may evolve in the future.

To evaluate the influence of glacial retreat upon coastal water column biogeochemistry we utilise stable oxygen isotopes and short-lived radium and thorium isotopes. Salinity and stable oxygen isotope measurements can be used to derive the magnitude and distribution of meteoric water (glacial melt and precipitation) and sea ice inputs (Meredith et al., 2008). Radium isotopes are associated with lithogenic inputs as they are products of thorium, which naturally occurs in rocks. Measurements of short-lived radium-224 and radium-223 isotopes (half-lives of = 3.6 and 11.4 days, respectively) and associated parent isotope activities such as thorium-228 (half-life 1.92 years) provide useful tracers for dissolved and particulate inputs of sedimentary material, respectively, in coastal regions over timescales of days to weeks. Radium and thorium measurements can therefore help to discriminate between inputs from benthic resuspension or sediment-rich meltwaters (Hendry et al., 2019). Studies tracing sedimentary inputs and fluxes using radiogenic radium isotopes at the WAP are sparse and often focussed on

groundwater (Annett et al., 2013; Dulaiova et al., 2009; Corbett et al., 2017; Null et al., 2019), rather than the circulation of meltwater-derived solutes.

Here we present derived freshwater contributions, radium and thorium isotope data, and macronutrient concentrations from contrasting land- and marine-terminating glacial fjords along the West Antarctic Peninsula collected during January 2020 on cruise JR19002 of RRS *James Clark Ross*.

## 2. Physical setting

The northern site (Marian Cove, 62° 13' S, 59° 46' W), situated on King George Island north of the Bransfield Strait (Fig. 1), is characterised by a 3.5 km long and 1.2 km wide inlet, <125 m deep, connecting to the deeper Maxwell Bay (< 600 m) via a steep sill (Fig. 2a). Marian Cove, and the adjacent Potter Cove, receive large volumes of meltwater drainage from the recently (since 2016) land-terminating Fourcade Glacier to the northeast (Falk et al., 2018). At Potter Cove, observational studies show that the rapidly retreating Fourcade glacier discharges approximately 20,700 m<sup>3</sup> d<sup>-1</sup> of glacier ice into the cove at a rate of 40 m a<sup>-1</sup>, and a comparable volume of meltwater drainage (Falk et al., 2016; Falk et al., 2018; Meredith et al., 2018). Available mean annual glacier frontal area loss rates for Marian Cove from 1978/79 to 2009/10 were 0.042 km<sup>2</sup> yr<sup>-1</sup> (Cook et al., 2016).

At the southern WAP, the Sheldon Glacier terminates within Sheldon Cove, Adelaide Island, Ryder Bay (67° 33' S, 68° 15' W, Fig. 1). The depth of Ryder Bay varies, with a central basin ~500 m deep (S-S2; Fig. 3a). Sheldon Cove feeds into the wider Ryder Bay over a steep sill at 200 m depth, sloping downwards to the central basin. From ice edge to outer station, Sheldon Cove is ~13.5 km long, and around 2.5 km wide. The mean annual frontal area loss rate for Sheldon Glacier 1978/79–2009/10 is 0.191 km<sup>2</sup> yr<sup>-1</sup> (Cook et al., 2016).

In Marian Cove, there were no observed icebergs or sea ice cover at the time of sampling. At Sheldon Cove, there was some sparse ice coverage. Landsat-1 satellite imagery reveals what appears to be a calving event at Sheldon Cove on 23/12/19, but at the point of sampling (13/01–18/01/20) there was very little remaining evidence of this glacial ice flux. Supplementary figs. S1 and S2 show Landsat-1 images of Marian Cove and Sheldon Cove, one week prior to sampling.

## 3. Methods

### 3.1. Hydrographic properties

Physical water column properties were measured with a SeaBird 911plus conductivity-temperature-depth (CTD) profiler, attached to a frame that also carried a rosette sampler with 24 20 L Niskin bottles. Discrete water samples were collected for analysis of salinity on a Guildline 8400B salinometer; no re-calibration of CTD conductivity was found necessary based on these data. We report CTD profiler potential temperature, transmission, and salinity. Transmission (%) represents the percentage of incident light that passes through an optical sensor fixed to the CTD and is used as an indicator of suspended material in the water column. Salinity is here presented on the Practical Salinity scale.

### 3.2. Radium

For radium samples from deeper than 1 m, 160 L per sample was collected by pooling multiple bottles on the CTD rosette. Surface samples (0–10 cm) of the same volume were collected from small boats by hand. Samples were passed through a column filled with ~20 g loosely-packed MnO<sub>2</sub>-coated fibre at a flow rate < 1 L min<sup>-1</sup>, at which soluble Ra adsorbs to the MnO<sub>2</sub> fibres at ~97% efficiency (Moore, 2008). The fibre was rinsed thoroughly with Milli-Q water to remove excess salts and particles, then dried to a moisture to fibre ratio of 0.6–1 g<sub>H2O</sub>:g<sub>fibre</sub>, according to methods in Sun and Torgersen (1998).

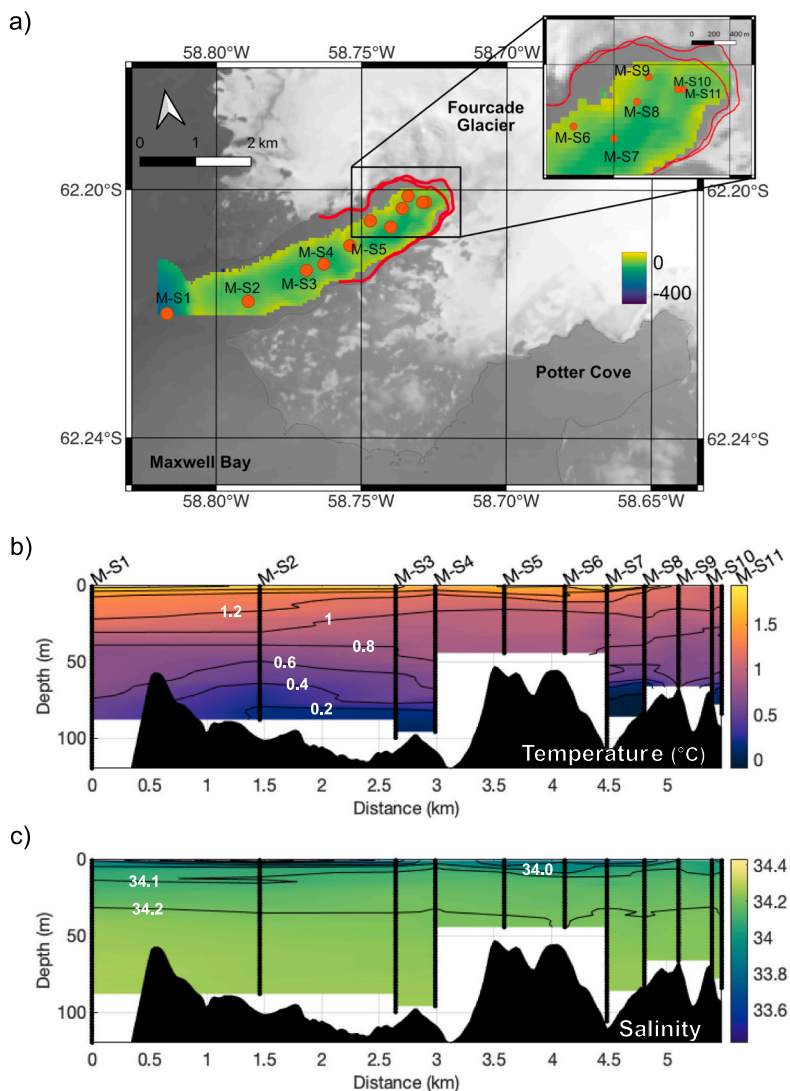


Fig. 2. a) Station map for Marian Cove, with multibeam echosounder data for bathymetry collected during the field study. Bathymetry overlies satellite imagery from Landsat 8 taken during the study period (USGS EROS), and along-track interpolated section profiles with depth for b) potential temperature and c) salinity at Marian Cove. Black dots in b) and c) represent sampling points.

Radium samples were analysed using the Radium Delayed Coincidence counting (RaDeCC) system as in Moore (2008). For first counts, counting was performed for 6–8 h as soon as possible after sampling, or until counts in the 220-channel exceed 400. Counting was performed again at ~21 days, and then at >90 days after sampling. These extra counts correct for  $^{224}\text{Ra}$  supported by  $^{228}\text{Th}$ , and  $^{223}\text{Ra}$  supported by  $^{227}\text{Ac}$ , respectively.

Count processing follows Garcia-Solsona et al. (2008), Moore (2008), Diego-Feliu et al. (2020) and Selzer et al. (2021) using the RaDeCC Reader program to convert counts to  $^{224}\text{Ra}$  activities in decays per minute (dpm). Standards of  $^{232}\text{Th}$ , in equilibrium with daughters to  $^{224}\text{Ra}$  of known activity (Annett et al., 2013) were measured several times to monitor detector efficiency throughout the study. The absolute activities of the 21-day count are used to estimate  $^{228}\text{Th}$ . We report excess  $^{224}\text{Ra}$  (herein  $^{224}\text{Ra}_{\text{XS}}$ ) and  $^{228}\text{Th}$  in this study.

### 3.3. Characterising freshwater inputs

Quantifying net freshwater inputs is possible using salinity measurements of seawater. To trace freshwater provenance, we

accompanied salinity measurements with stable oxygen isotopes ( $\delta^{18}\text{O}$ , the standardised ratio of  $^{18}\text{O}$  to  $^{16}\text{O}$  in seawater). In surface waters,  $\delta^{18}\text{O}$  reflects the magnitude and distribution of freshwater inputs, whilst in the ocean interior,  $\delta^{18}\text{O}$  is a conservative tracer. Distinctions of freshwater sources using  $\delta^{18}\text{O}$  arise because, whilst the salinity of precipitation is invariant with latitude, the  $\delta^{18}\text{O}$  of precipitation becomes lower towards the poles due to preferential evaporation of the lighter isotope and preferential rainout of the heavier isotope. Therefore,  $\delta^{18}\text{O}$  is very low in high latitude precipitation (–10 to –20‰ in coastal Antarctica) and can be extremely low in glacial ice (e.g. as low as –50‰) (Weiss et al., 1979), providing a useful tracer of glacial discharge into the ocean (Schlosser et al., 1990). Conversely, whilst the influence of sea ice formation and melt impacts salinity considerably through brine rejection and freshwater release, it has minimal impact upon  $\delta^{18}\text{O}$  (Meredith et al., 2008). Concurrent measurements of salinity and  $\delta^{18}\text{O}$  can therefore separate sea ice melt from meteoric water (precipitation and glacial melt) contributions, with respect to the ambient seawater.

From the CTD/Niskin bottle casts, approximately eight samples were collected per deployment for  $\delta^{18}\text{O}$ , with increased depth resolution in the near-surface layers to resolve the freshwater gradients. Samples



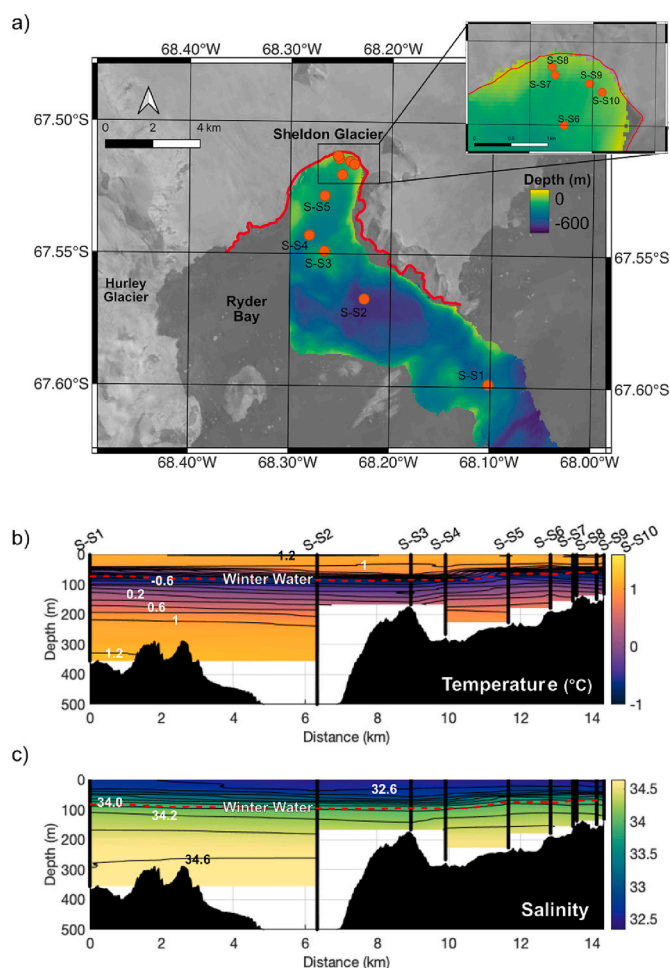


**Fig. 3.** a) Station map, for Sheldon Cove, with multibeam echosounder data for bathymetry collected during the field study. Bathymetry overlies satellite imagery from Landsat 8 taken during the study period (USGS EROS). Along-track interpolated section profiles with depth for b) Potential temperature and c) Salinity. Black dots in b) and c) represent sampling points. The red dotted line represents the Winter Water layer foci. (For interpretation of the references to colour in this figure legend, the reader is referred to the web version of this article.)

were collected and stored in 50 mL glass vials rinsed with sample water; these were sealed with rubber stoppers and crimp seals. Surface samples (~0–10 cm) were collected from small rigid inflatable boats using the same protocol. Oxygen isotope samples were analysed ~9 months later

**Table 1**

Given salinity and  $\delta^{18}\text{O}$  endmember values for each endmember used in analysis during this study. References for the endmember values are provided.

	Sheldon Cove	Marian Cove
<i>Salinity</i>		
Sea ice melt	7	5
Meteoric water	0	0
mCDW	34.62	34.40
$\delta^{18}\text{O}$ (‰)		
Sea ice melt	2.1	1.6
Meteoric water	-16	-11
mCDW	0.04	-0.2
References	Meredith et al. (2017) and references therein	Meredith et al. (2018)

at the UK's National Environmental Isotope Facility at the British Geological Survey, using the  $\text{CO}_2$  equilibration method (Epstein and Mayeda, 1953) with an Isoprime 100 mass spectrometer plus Aquaprep device. Isotope measurements were calibrated against internal and international standards including VSMOW2 and VSLAP2. Based on duplicate analysis, analytical reproducibility was ~0.02 %.

A simple three-endmember mass balance method was employed to quantify the contributions of meteoric water, sea ice melt and regional deep water, developed by Östlund and Hut (1984) and adapted for use at the WAP by Meredith et al. (2008) and Meredith et al. (2010). We report  $f_{\text{sim}}$ ,  $f_{\text{met}}$  and  $f_{\text{sw}}$  as the fraction (%) of sea ice melt, meteoric water, and seawater endmember contribution, respectively. Determining realistic freshwater contributions requires accurate choices for endmember (undiluted) values. Endmember values used follow those in Meredith et al. (2017) and Meredith et al. (2018) and are given in Table 1. Most endmember values in the region are clearly established, and derivation is described in Meredith et al. (2008) and Meredith et al. (2010). The largest uncertainty propagated in the determination of fractional freshwater contributions is from the mean meteoric water  $\delta^{18}\text{O}$  endmember, as a combination of glacial meltwater and local precipitation, which both vary spatially and temporally in oxygen isotope value. Sensitivity studies find that the uncertainties in the final freshwater fractions are better than 1% for point values Meredith et al. (2008) and Meredith et al. (2010).

### 3.4. Macronutrients sampling

Macronutrient samples were collected from the CTD rosette at a frequency of 8–10 depths for each profile, with increased resolution in the mixed layer where salinity gradients are largest. Samples were filtered in-line into clean Nalgene HDPE 60 mL bottles, using a 0.2  $\mu\text{m}$  AcroPak™ 200 filter capsule. Surface samples were collected from small boats into clean Nalgene HDPE bottles, and then filtered offline using the same method. All samples were frozen immediately at  $-20^\circ\text{C}$ .

Samples were analysed 8 months after collection at the Plymouth Marine Laboratory (UK) using a 5-channel segmented flow colorimetric SEAL Analytical AAIII autoanalyser for nitrate + nitrite, nitrite, phosphate and silicic acid. The analytical methods were as described in Woodward and Rees (2001), and samples were analysed along with certified nutrient reference materials (Batch BV; KANSO Technos, Japan), to confirm data quality and analytical confidence. Reactive silica polymerizes when frozen, especially at high concentrations as found here, and so prior to analysis, samples were thawed for 45 min in a  $50^\circ\text{C}$  water bath and returned to room temperature for 45 min to ensure complete depolymerization and complete recovery of the reactive silica (Becker et al., 2020). Samples standard deviation was generally better than 4%. Nitrate concentrations are given as the difference between nitrate + nitrite and nitrite measurements.

### 3.5. Determining macronutrient fluxes from shelf or surface sources

Gradient profiles of  $^{224}\text{Ra}_{\text{XS}}$  can be used to quantify the macronutrient flux from sedimentary sources, such as from shelf resuspension or meltwater inputs (Dulaiova et al., 2009). In a system dominated by eddy diffusion, the distribution of  $^{224}\text{Ra}_{\text{XS}}$  will depend only on the radioactive decay of the isotope and water mass mixing. Therefore, the gradient of  $\ln(^{224}\text{Ra}_{\text{XS}})$  with distance will depend only on the decay constant ( $\lambda$ ) and the eddy diffusion coefficient ( $K_h$ ) (Moore, 2000). If the role of advection is significant, the slope in  $\ln(^{224}\text{Ra}_{\text{XS}})$  profiles would be either concave or convex, rather than linear. We therefore only use profiles with a linear relationship with distance. Derivation of the eddy diffusion coefficient  $K_h$  ( $\text{m}^2 \text{s}^{-1}$ ) was performed as in Moore (2000) and Dulaiova et al. (2009) as:

$$\text{slope} = \sqrt{\frac{\lambda_{224}}{K_h}} \quad (1)$$



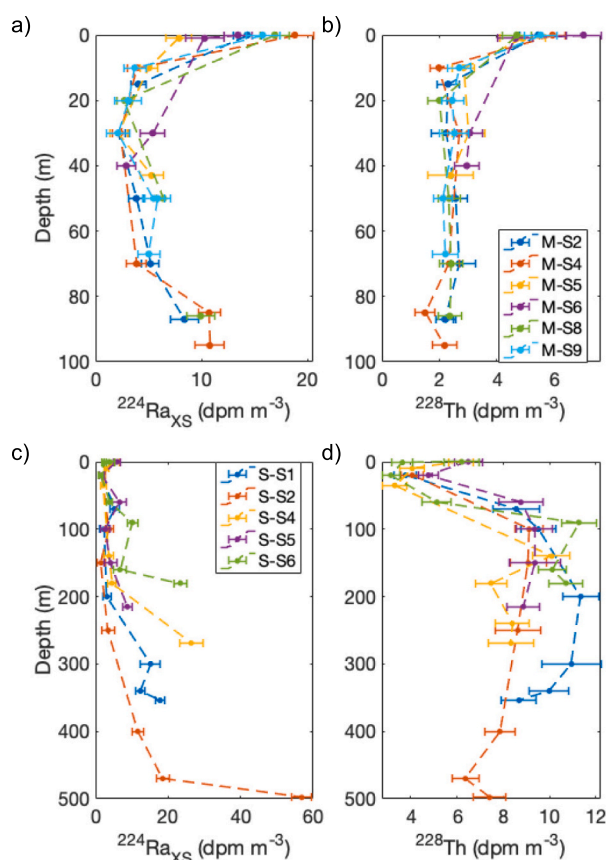


**Fig. 4.** a) Radium-224 and b) Thorium-228 depth profiles for Marian Cove; c) Radium-224 and d) Thorium-228 depth profiles for Sheldon Cove. Error bars are calculated using the count processing methods given in Section 3.2.

where the slope is for  $\ln(^{224}\text{Ra}_{\text{XS}})$  with distance ( $x$ ), and  $\lambda_{224}$  is the decay constant for radium-224 ( $2.21 \times 10^{-6} \text{ s}^{-1}$ ). Multiplying the derived  $K_h$  with the change in  $^{224}\text{Ra}_{\text{XS}}$  over depth ( $\frac{d(^{224}\text{Ra})}{dx}$ ,  $\text{mmol m}^{-4}$ ) gives the  $^{224}\text{Ra}_{\text{XS}}$  flux ( $\text{dpm m}^{-2} \text{ s}^{-1}$ ) associated with the sediment supply. Then, multiplying this flux by the ratio of nutrient: $^{224}\text{Ra}_{\text{XS}}$  provides the macronutrient flux, which we report in  $\text{mmol m}^{-2} \text{ d}^{-1}$ .

In Ryder Bay, where the glacier has a marine-terminating grounding line, these depths were measured acoustically using the Kongsberg EM122 multibeam echosounder, hull-mounted on RRS *James Clark Ross*.

## 4. Results

### 4.1. Water mass properties

Fig. 2 shows station transect and depth profiles at Marian Cove. Water temperature decreases with depth, to a minimum of  $-0.096 \text{ }^\circ\text{C}$  at station M-S7 (Fig. 2b). At depth, temperature increases with distance from the glacier terminus to an outer station maximum of  $0.005 \text{ }^\circ\text{C}$  at M-S1. Salinity (S) increases with depth, with a strong vertical gradient in the top 40 m, from 34.02 to 34.37 (Fig. 2c). There is a positive S gradient from glacier proximity to the outer bay, with a maximum at M-S1 at 229 m of 34.60.

At Sheldon Cove, waters deeper than 350 m were  $0.8\text{--}1.2 \text{ }^\circ\text{C}$ , representing warm mCDW shelf water. The surface water temperature decreased rapidly with depth from a maximum of  $1.3 \text{ }^\circ\text{C}$ , representing the Antarctic Surface Water (AASW), to a temperature minimum zone ( $\geq -0.85 \text{ }^\circ\text{C}$ ) at 55 m at stations proximal to the ice edge, deepening to 70–90 m at the 3 outer stations. The cold layer represents the Winter Water layer, a term given to the summertime remnant of the deep winter

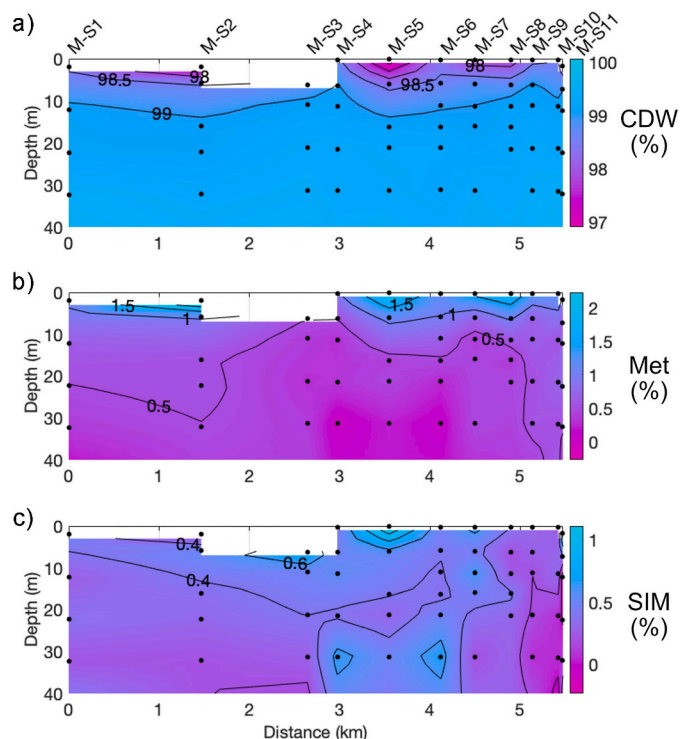


**Fig. 5.** Interpolated section profiles for percentage contributions from a) CDW b) Meteoric water and c) Sea ice melt within the top 40 m of the water column at Marian Cove.

surface mixed layer (Fig. 3b). Strong stratification is apparent throughout the cove, driven by the salinity and freshwater distribution, with marked thermo- and haloclines above the Winter Water (Fig. 3c).

The warm mCDW layer at Sheldon Cove contrasts with the colder waters in the northern Marian Cove where shelf incursions of mCDW are  $\sim 0 \text{ }^\circ\text{C}$ . Cook et al. (2016) observed mean temperatures of modified CDW shelf waters are warmer in the south WAP ( $> 1 \text{ }^\circ\text{C}$ , 1945–2009), relative to the north ( $< 0 \text{ }^\circ\text{C}$ , 1945–2009), where there is a greater influence of cold Weddell Sea waters (Dotto et al., 2016).

### 4.2. $^{224}\text{Ra}_{\text{XS}}$ and $^{228}\text{Th}$ profiles as indicators of sediment inputs

Fig. 4 shows the depth profiles across Sheldon Cove and Marian Cove for  $^{224}\text{Ra}_{\text{XS}}$  and  $^{228}\text{Th}$  with associated propagated errors. Raw data for  $^{224}\text{Ra}_{\text{XS}}$  and  $^{228}\text{Th}$  is provided in Supplementary 1.1. At Marian Cove,  $^{224}\text{Ra}_{\text{XS}}$  and  $^{228}\text{Th}$  activities in the top 0–1 m diverge from lower activities in the subsurface water column (Fig. 4 a, b). Small boat  $^{224}\text{Ra}_{\text{XS}}$  samples (0–10 cm) range from  $13.4$  to  $18.8 \text{ dpm m}^{-3}$ , and the shallowest CTD  $^{224}\text{Ra}_{\text{XS}}$  samples ( $\sim 1 \text{ m}$ ) were  $7.9$  and  $10.2 \text{ dpm m}^{-3}$ . This surface increase in  $^{224}\text{Ra}_{\text{XS}}$  activity was concurrent with a decrease in S of  $\sim 1.0$ , indicating a distinct, fresher, and sediment-laden water layer in the top 0–10 cm. The  $^{224}\text{Ra}_{\text{XS}}$  activity increased again with proximity to the seafloor at Marian Cove, to a maximum of  $10.8 \text{ dpm m}^{-3}$  in the centre of the cove at M-S4. The highest activity benthic samples ( $< 20 \text{ m}$  from the seafloor) were at M-S4 and M-S2, the furthest stations from the glacier edge before the sill. The increase in  $^{224}\text{Ra}_{\text{XS}}$  at the benthic boundary at Marian Cove provides evidence for a sedimentary-derived dissolved load within the water column. Thorium-228 activities were also enhanced in the surface samples ( $\leq 1 \text{ m}$ ,  $4.6\text{--}7.0 \text{ dpm m}^{-3}$ ), but not at depth, suggesting little variability in the suspended particle load below the surface meltwater layer.

At Sheldon Cove,  $^{224}\text{Ra}_{\text{XS}}$  ranged from  $1.4$  to  $56.8 \text{ dpm m}^{-3}$  ( $\bar{x} = 8.4 \pm 10.6 \text{ dpm m}^{-3}$ , Fig. 4 c, d). The highest activities in each profile were found near ( $\leq 20 \text{ m}$ ) the benthic boundary layer, with a maximum value

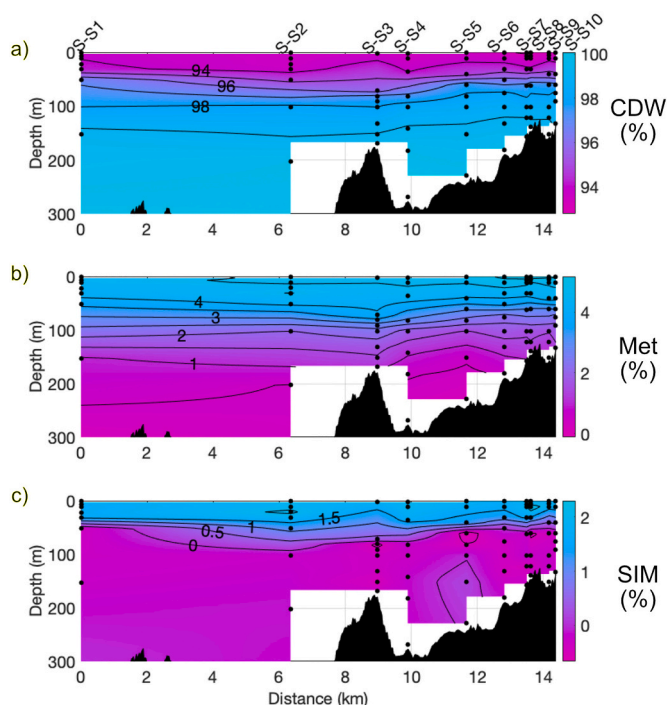


**Fig. 6.** Interpolated section profiles for percentage contributions from a) CDW b) Meteoric water and c) Sea ice melt within the top 40 m of the water column at Sheldon Cove.

of  $56.8 \text{ dpm m}^{-3}$  at S—S2. This is, to the best of our knowledge, two times higher than any other water column  $^{224}\text{Ra}_{\text{XS}}$  activity measured in Antarctic waters. Generally, samples  $>20 \text{ m}$  from the seafloor were much lower in activity, averaging  $5.4 \pm 4.2 \text{ dpm m}^{-3}$  ( $n = 31$ ). The stations furthest from the ice edge (S—S1 and S—S2, 14.2 and 8 km respectively) exhibit the highest mean subsurface  $^{224}\text{Ra}_{\text{XS}}$  activities.

Thorium-228 activities also show variability throughout the water column at Sheldon Cove, ranging from  $3.1$  to  $11.4 \text{ dpm m}^{-3}$ , with a mean of  $8.7 \pm 5.9 \text{ dpm m}^{-3}$ . The highest  $^{228}\text{Th}$  activities were observed across  $90$ – $180 \text{ m}$  at S—S6 ( $10.1$ – $11.3 \text{ dpm m}^{-3}$ ) and at  $200 \text{ m}$  at S—S1 ( $11.4 \text{ dpm m}^{-3}$ ), with mid-depth enrichment in  $^{228}\text{Th}$  seen across all profiles. To our knowledge, these activities are three-fold higher than any  $^{228}\text{Th}$  previously published from water column Antarctic studies (Dulaiova et al., 2009; Null et al., 2019; Corbett et al., 2017; Annett et al., 2013). The strong  $^{228}\text{Th}$  signal observed in the mid-depths ( $> 40 \text{ m}$ ) is not reflected in the subsurface  $10$ – $35 \text{ m}$  layer, indicating a reduced influence of particulates within that layer. The overall benthic signals in  $^{224}\text{Ra}_{\text{XS}}$  and  $^{228}\text{Th}$  were significantly higher with respect to MC.

#### 4.3. Freshwater contributions to the water column

Using salinity and  $\delta^{18}\text{O}$ , we present the percentage contributions of meteoric water ( $f_{\text{met}}$ ) and sea ice melt ( $f_{\text{sim}}$ ), using mCDW as the ambient oceanic water mass (Fig. 5). Within the top  $10 \text{ m}$  at Marian Cove, the meteoric water contribution ranges from  $0.7$  to  $13.0\%$ , which is to our knowledge the highest meltwater contribution measured at the West Antarctic Peninsula. Samples collected using small boats ( $0$ – $10 \text{ cm}$ ) range from  $2.3$  to  $13.0\%$  ( $n = 24$ ,  $\bar{x} = 5.8\%$ ), whilst surface CTD samples ( $\sim 1 \text{ m}$ ) range from  $0.7$  to  $2.7\%$ . For water depths below  $10 \text{ m}$ ,  $f_{\text{met}}$  for all but one sample is  $<1\%$ , demonstrating a steep negative gradient in the top  $10 \text{ m}$  of the water column. Small boat samples are from a shallower and less disturbed surface water layer compared to the CTD samples, which may have undergone some mixing from the research vessel and rosette deployment. Meteoric contributions drive strong stratification in the top  $10 \text{ m}$ , and  $f_{\text{sim}}$  is comparatively low in surface waters, at an average of  $0.65\%$ . The well-mixed subsurface water column at Marian

Cove suggests that the shallow nature of the cove permits winter mixing to the seabed.

Sheldon Cove exhibits a larger total contribution of freshwater, greatest in the surface waters and persisting to  $>100 \text{ m}$  depth for both  $f_{\text{met}}$  and  $f_{\text{sim}}$  (Fig. 6). The meteoric contribution above the minimum potential temperature,  $\theta_{\text{min}}$ , represents inputs since the previous winter. Evaluating CTD profiles above  $\theta_{\text{min}}$  produces a mean  $f_{\text{met}}$  of  $4.2 \pm 0.8\%$ , with a maximum contribution of  $5.2\%$ . Small boat samples from the top  $10 \text{ cm}$  range from  $5.6$  to  $7.4\%$  for  $f_{\text{met}}$  ( $n = 15$ ,  $\bar{x} = 6.1\%$ ). Sea ice provides a comparatively lower contribution of  $1.2 \pm 0.9\%$  within the surface mixed layer.

#### 4.4. Macronutrients

Fig. 7 a-c shows section profiles of Marian Cove for nitrate ( $\text{NO}_3^-$ ), phosphate ( $\text{PO}_4^{3-}$ ) and silicic acid ( $\text{Si}(\text{OH})_4$ ) concentrations. Macronutrients  $\text{NO}_3^-$ ,  $\text{PO}_4^{3-}$  and  $\text{Si}(\text{OH})_4$  were generally replete and increasing with depth, although there is considerable variation between stations, such as between M-S5, M-S6 and M-S7 for  $\text{Si}(\text{OH})_4$ . This increase with depth provides evidence for a common bottom water source, such as modified Bransfield Strait water. However, the high local variability for macronutrient concentrations at Marian Cove, particularly with proximity to the glacier, suggests some alternative controls upon the distributions. Fig. 8 a-c shows equivalent macronutrient section profiles for Sheldon Cove. The vertical stratification shown in the hydrographic profiles (Fig. 3 b,c) was reflected in macronutrient concentrations, with a steep nutricline at around  $80$ – $100 \text{ m}$  observed across the cove. Coupling this with the hydrography of Sheldon Cove indicates that mCDW dominated macronutrient supply, in line with previous observations at the southern WAP (Henley et al., 2017). Variability in macronutrients was lower at Sheldon Cove but increased with proximity to the ice edge. Notably, enrichment in  $\text{Si}(\text{OH})_4$  was observed at depth at S—S4 and the adjacent S—S7 and S8, that was not reflected in other nutrient profiles. Nitrite ( $\text{NO}_2^-$ ) concentrations for both bays are provided in Supplementary Fig. S3 and S4.

## 5. Discussion

### 5.1. Tracing the influence of sediments at Marian Cove

Analysis of both small boat and CTD samples at Marian Cove indicates a strong negative linear correlation between both  $^{224}\text{Ra}_{\text{XS}}$  and  $S$  ( $r^2 = 0.64$ ,  $p \leq 0.001$ ), and  $^{228}\text{Th}$  and  $S$  ( $r^2 = 0.76$ ,  $p \leq 0.001$ ), indicating that inputs of freshwater, predominantly meteoric water, provide a source of both dissolved and particulate material to the cove surface waters. The relationship is driven by surface waters, which diverge from the subsurface ( $> 1 \text{ m}$ ) in both salinity and radioisotope activity (Fig. 9a, b):  $^{224}\text{Ra}_{\text{XS}}$  was  $\sim 3.6$  times greater at the surface than the water column average. The marked decrease in transmission in the upper  $10 \text{ m}$  (Fig. 9c) supports this interpretation. The use of radium and thorium provides more robust evidence of sustained particle and dissolved solute supply than using only transmission, as transmission does not distinguish between organic and inorganic material or dissolved and suspended particulate matter. We conclude that a prominent sediment-rich lens of freshwater persists across the cove, indicative of surface injection of turbid meltwater from glacial runoff. The hydrography and radium activities at Marian Cove in this study indicate a well-mixed water column, with a modest increase in radium activities near the benthic boundary indicating the presence of benthic exchange, but rapid dispersion of this signal over short distances.

### 5.2. Controls on macronutrient distribution at Marian Cove

Typically, biogeochemistry studies along the West Antarctic Peninsula present strong coupling of nitrate and phosphate due to the common mCDW source (Henley et al., 2017). However, at Marian Cove,

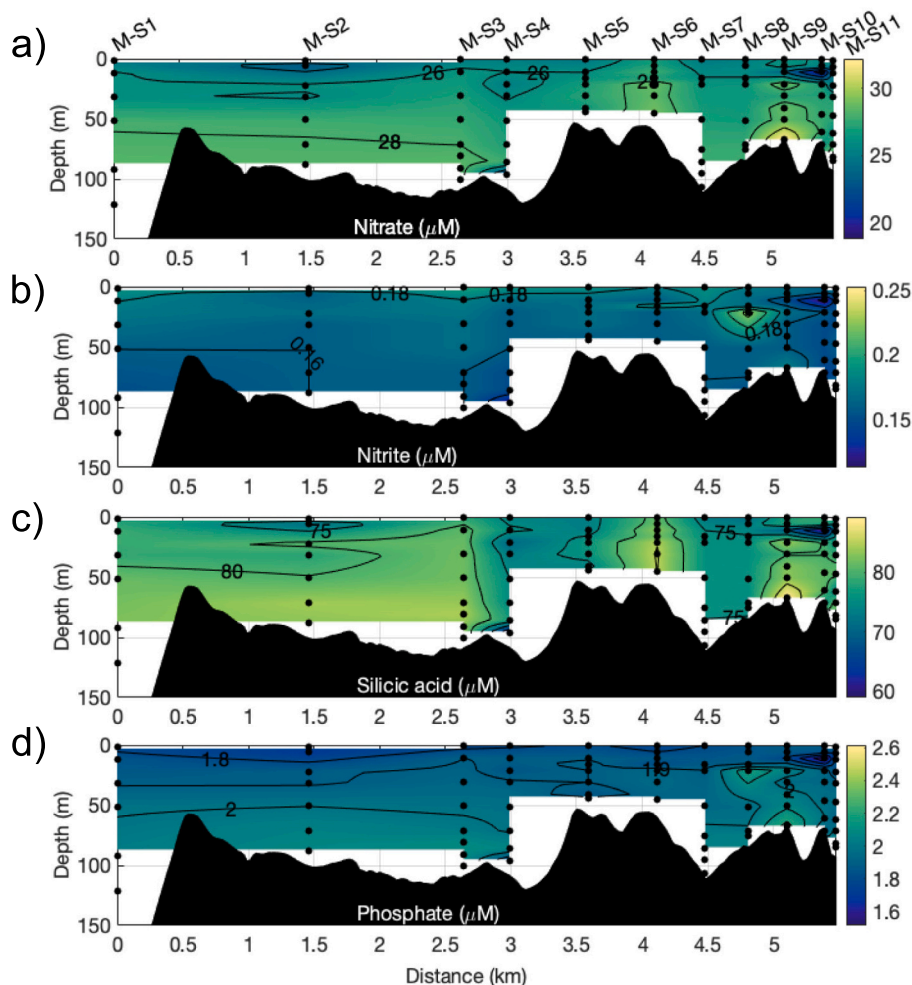


**Fig. 7.** Section profiles with distance along track for macronutrients a) Nitrate, b) Phosphate, and c) Silicic acid at Marian Cove. Data is interpolated with depth, along track from the distal station (0 km) towards the ice-front proximal stations.

regression analysis of  $\text{NO}_3^-$  and  $\text{PO}_4^{3-}$  gives an  $r^2 = 0.38$  and a  $\text{NO}_3:\text{PO}_4^{3-}$  of 13.8, demonstrating differing controls upon  $\text{NO}_3^-$  and  $\text{PO}_4^{3-}$  concentrations and an N:P ratio below Redfield. Nitrate to silicic acid is more tightly coupled ( $r^2 = 0.71$ ) with a mean  $\text{Si}(\text{OH})_4:\text{NO}_3^-$  of 2.4, see Supplementary Fig. S5.

Although we can quantify benthic vertical fluxes of  $^{224}\text{Ra}_{\text{XS}}$  at Marian Cove, these were not concurrent with macronutrient concentration gradients. In the Bransfield Strait region, strong katabatic winds can influence mixing down to the seabed, whilst tides also exert influence over circulation during comparatively weaker wind forcing. These processes can resuspend sediments in these shallow regions, both through horizontal and vertical circulation, enhancing upwelling (Schloss et al., 1997). Considering both the narrow width and shallow depth of the cove, it is possible that macronutrient fluxes at the sediment-water interface at Marian Cove are both vertical and horizontal, or indeterminable from the vertical resolution of our radium isotope depth profiles, and therefore not captured here. Furthermore, the narrow and shallow cove geometry, coupled with strong wind events, would likely drive relatively rapid flushing of the cove, which is perhaps not captured on the timescales used here to determine fluxes.

### 5.3. Impacts of glacial melt on Marian Cove biogeochemistry

The corresponding high  $^{224}\text{Ra}_{\text{XS}}$  and  $^{228}\text{Th}$  activities in Marian Cove surface waters are the highest recorded in Antarctic coastal surface waters and suggest a high sediment load carried by the meteoric water.

We would expect extremely low (or negligible)  $^{224}\text{Ra}_{\text{XS}}$  activities in polar precipitation, so it is reasonable to conclude that glacial inputs dominate the meteoric fraction. Marian Cove is fed by glacial surface melt and subglacial meltwater from the Fourcade Glacier to the northeast. Studies on the adjacent Potter Cove, fed by the same glacier, corroborate our results of a turbid and comparably fresh thin surface water layer (Meredith et al., 2018). Turbid surface meltwater can adversely impact local productivity by reducing light penetration into the water column and limiting both benthic and pelagic primary production, as observed in Potter Cove (Hoffmann et al., 2019). Primary producers that prevail in these conditions are typically adapted to low-light conditions, and strong bloom events are rare: physical conditions such as intense winds and reduced irradiance due to high particle loads historically limit productivity in the region (Schloss et al., 2014). Moreover, a study of the impact of high sedimentation rates upon marine benthos in Potter Cove indicates major shifts in species composition, abundances and community structure, with a general loss in diversity over 20 years due to sedimentation tolerance limits (Sahade et al., 2015).

Using the stations sampled in darkness to remove ambient light effects, we analysed the fluorescence data for the top 100 m of Marian Cove (M-S4 and M-S9) and Sheldon Cove (S-S6 and S-S7). Fluorescence data was captured by a fluorometer sensor attached to the CTD frame, calibrated using the inbuilt SeaBird pre-processing capability. Fluorescence data was not calibrated in-situ and so we expect some drift to have occurred since calibration pre-cruise. For Marian Cove, the



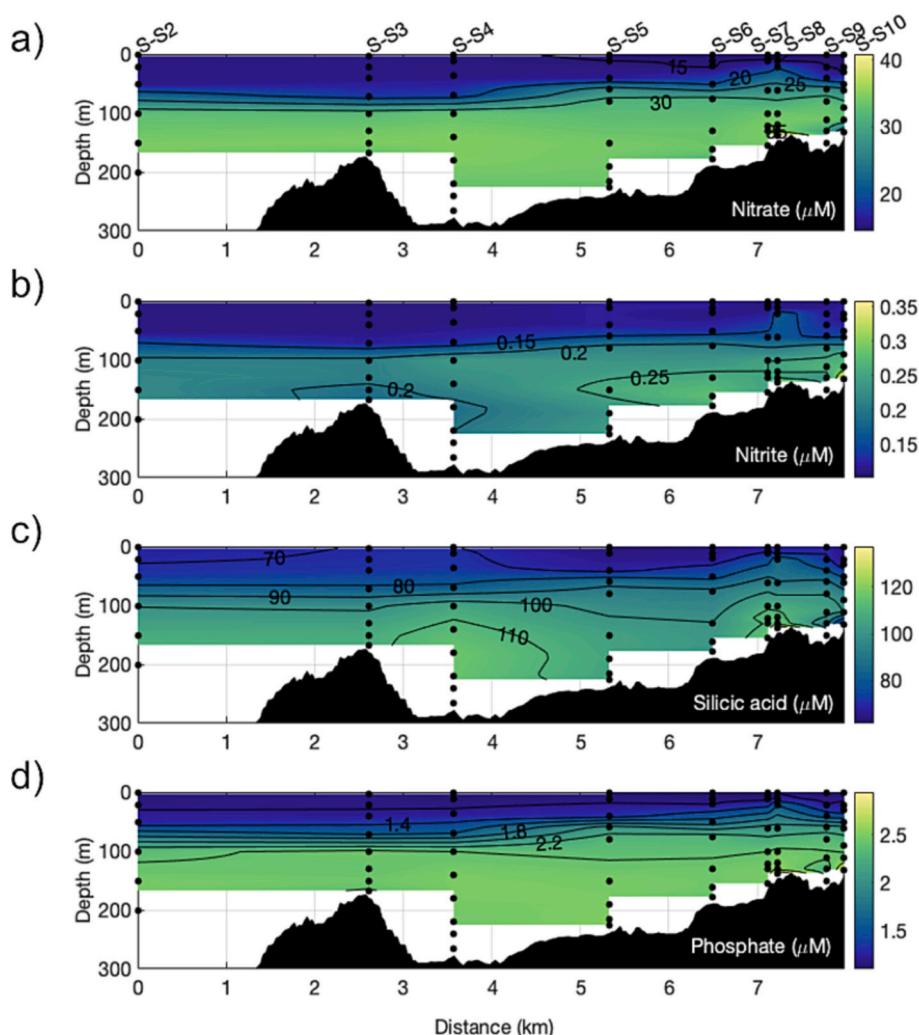


**Fig. 8.** Section profiles with distance along track for macronutrients a) Nitrate, b) Phosphate, and c) Silicic acid at Sheldon Cove. Data is interpolated with depth, along track from the distal station (0 km) towards the ice-front proximal stations.

median and maximum fluorescence values were  $0.047$  and  $0.37 \mu\text{g L}^{-1}$ , respectively, compared to higher values of  $0.19$  and  $0.69 \mu\text{g L}^{-1}$  for Sheldon Cove (see Supplementary Fig. S6). Stations S—S7 and M-S9 are both relatively similar in position in the coves, proximal to the glacier edge, and show considerable difference in fluorescence ( $0.65 \mu\text{g L}^{-1}$  compared to  $0.17 \mu\text{g L}^{-1}$ , respectively). The relative difference observed in the CTD fluorometer data suggests that phytoplankton standing stock was markedly lower at Marian Cove. Macronutrient profiles showed replete concentrations at both coves, and micronutrient concentrations tend to be high at the coastal WAP (Annett et al., 2017; Bown et al., 2018). The impact of sediment upon light availability is therefore the most likely cause of lower productivity at Marian Cove from the available data.

The impact of a rising prevalence of land-terminating glaciers at the WAP should be considered in the context of an increase in sediment-laden injection into surface waters. Our findings suggest the flux of high sediment loads to a nutrient-replete region such as Marian Cove will result in a reduction in net primary production as a result of perturbations to light availability (Ferreira et al., 2020). The accompanied high turbidity may limit uptake of macronutrients by primary producers, as shown in Holding et al. (2019). Subsequently, unused nutrients may be exported further offshore, fuelling productivity downstream. Increases in primary production further offshore will in turn influence productivity throughout the Southern Ocean food web, and the efficiency of ocean carbon uptake in the region.

#### 5.4. The interaction between sediments and macronutrients at Sheldon Cove

In contrast with Marian Cove, both  $^{224}\text{Ra}_{\text{XS}}$  and  $^{228}\text{Th}$  correlate with increasing salinity and depth at Sheldon Cove (Fig. 10 a, b). Elevated  $^{224}\text{Ra}_{\text{XS}}$  activities of up to  $56.9 \text{ dpm m}^{-3}$  proximal to the seafloor provide clear evidence for high dissolved loads persisting across the study area (Maiti et al., 2015). Thorium-228 activities are elevated in the mid-depths across the bay but tend to be reduced near the seafloor. Scavenging of  $^{228}\text{Th}$  by sinking particles at depth is a commonly observed process, which could explain the downturn in  $^{228}\text{Th}$  in the profiles at depth. Quantification is not possible with the available data, but the presence of fine sediments or large volumes of sediment would generally increase scavenging rates of  $^{228}\text{Th}$  (Cochran and Masqué, 2003; Broecker et al., 1973). As such, we investigated the influence of benthic mixing at the seafloor and near to the glacier, the source of the high particle signal that persists across the bay, and the influence on macronutrient distributions.

The positive correlation between macronutrient concentrations and mCDW contribution at Sheldon Cove indicates that mCDW is the main macronutrient source ( $r^2 = 0.94, 0.95$  and  $0.89$  for  $\text{NO}_3^-$ ,  $\text{PO}_4^{3-}$  and  $\text{Si}(\text{OH})_4$  respectively). However, the greater enrichment of  $\text{Si}(\text{OH})_4$  at depth relative to  $\text{NO}_3^-$  (Fig. 8) is evidence for an additional source of silicic acid in Sheldon Cove.

We used  $^{224}\text{Ra}_{\text{XS}}$  to determine the potential vertical fluxes of

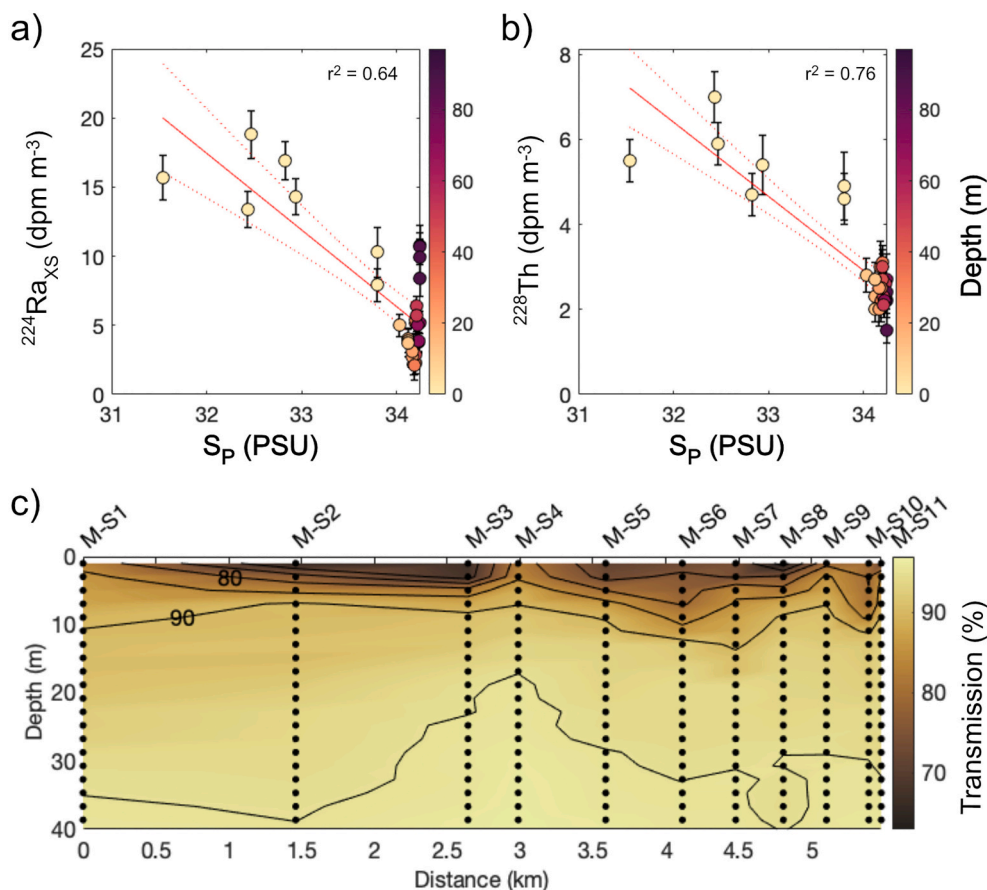


**Fig. 9.** Short-lived radiogenic isotope activities plotted with salinity, shaded with depth for a)  $^{224}\text{Ra}_{\text{XS}}$  and b)  $^{228}\text{Th}$  at Marian Cove. The red line and dotted red lines indicate the linear regression and 95% confidence intervals, respectively; r-squared values are shown on each subplot c) Transmission data for the top 40 m along-track for Marian Cove. (For interpretation of the references to colour in this figure legend, the reader is referred to the web version of this article.)

macronutrients from the shelf at Sheldon Cove, and then inferred whether these are driven by benthic fluxes, as observed for  $\text{Si}(\text{OH})_4$  in glacial fjords (e.g. Cassarino et al., 2020; Ng et al., 2020) or nutrient entrainment by buoyant meltwater, which would be exhibited in all macronutrient profiles (e.g. Meire et al., 2017). At S–S2, S–S4, S–S5 and S–S6 a linear relationship was observed between  $\ln(^{224}\text{Ra}_{\text{XS}})$  and depth, reaching a minimum (1.34–2.19  $\text{dpm m}^{-3}$ ) in the first samples below the thermocline. By plotting  $\ln(^{224}\text{Ra}_{\text{XS}})$  with macronutrients, the strongest linear coupling is observed at S–S6 for  $\text{Si}(\text{OH})_4$ ,  $\text{NO}_3^-$  and  $\text{PO}_4^{3-}$  ( $r^2 = 0.99$ ,  $0.99$  and  $0.98$ , respectively), and at S–S2, for only  $\text{Si}(\text{OH})_4$  ( $r^2 = 0.96$ ; See Supplementary Fig. S6). Vertical flux parameters at S–S2, S–S4 and S–S6 are provided in Table 2.

At S–S2, located in a deep region of the cove, distal from the ice edge, the change in  $^{224}\text{Ra}_{\text{XS}}$  upwards correlates with  $\text{Si}(\text{OH})_4$ , giving a vertical flux of  $0.038 \text{ mmol m}^{-2} \text{ d}^{-1}$  for  $\text{Si}(\text{OH})_4$  ( $\text{slope}_{\ln(^{224}\text{Ra})} = 0.008$ ,  $r^2 = 0.999$ ). At S–S4, on the glacier side of the sill, the  $^{224}\text{Ra}_{\text{XS}}$  fluxes resolve a greater vertical  $\text{Si}(\text{OH})_4$  flux of  $0.12 \text{ mmol m}^{-2} \text{ d}^{-1}$  ( $\text{slope}_{\ln(^{224}\text{Ra})} = 0.005$ ,  $r^2 = 0.96$ ). At S–S6, vertical fluxes are  $0.1$ ,  $0.06$ , and  $0.004 \text{ mmol m}^{-2} \text{ d}^{-1}$  for  $\text{Si}(\text{OH})_4$ ,  $\text{NO}_3^-$  and  $\text{PO}_4^{3-}$ , respectively. The fluxes calculated for  $\text{Si}(\text{OH})_4$  at S–S2 and S–S4 are broadly comparable with previous studies on diffusive porewater-benthic boundary fluxes in glacial fjords that use Fick's law of diffusion. These studies report fluxes of  $0.24$ – $0.25 \text{ mmol m}^{-2} \text{ d}^{-1}$  along the WAP (Cassarino et al., 2020), and  $0.3$ – $3 \text{ mmol m}^{-2} \text{ d}^{-1}$  on the glacially influenced Greenland shelf (Ng et al., 2020). The higher flux of  $\text{Si}(\text{OH})_4$  at S–S4 is three times higher than that calculated at S–S2, potentially due to the northward flow of deep mCDW over the sill to the south inducing dynamic resuspension of shelf sediments. The flow of water over coastal sills can enhance mixing, sediment resuspension and water entrainment (e.g. Venables et al.,

2017). This highlights the importance of regional bathymetry in the resuspension and input of  $\text{Si}(\text{OH})_4$  and other porewater-derived (micro) nutrients, such as iron, to the water column.

Vertical macronutrient flux calculations using  $^{224}\text{Ra}_{\text{XS}}$  highlights deep-water sources of  $\text{Si}(\text{OH})_4$  at S–S2 and S–S4, which are decoupled from  $\text{NO}_3^-$  and  $\text{PO}_4^{3-}$ . However, at S–S6, a common mechanism drives the vertical flux of  $\text{Si}(\text{OH})_4$ ,  $\text{NO}_3^-$  and  $\text{PO}_4^{3-}$ . Considering the proximity of S–S6 to the glacier terminus, we infer that the vertical macronutrient flux over 90–20 m is evidence for entrainment of macronutrient-rich mCDW by buoyant glacial melt. On point of melting the water would advect horizontally, whilst rapidly rising to achieve neutral buoyancy, entraining mCDW upwards.

##### 5.5. The influence of Sheldon Cove meltwater upon biogeochemistry

Fig. 11 shows the relationship between potential temperature, salinity, with depth and transmission for the whole of Sheldon Cove (Fig. 11 a, b), compared with stations proximal to the glacier front (Fig. 11 c,d). Also plotted is the Gade Line (Gade, 1979), defined as the  $\theta$ - $S$  mixing relationship of ambient seawater and glacial melt (melted at the glacier face by the warm ambient seawater). Generally speaking, Sheldon Cove exhibits a  $\theta$ - $S$  profile typical of glaciated bays along the West Antarctic Peninsula, where mCDW mixes with Winter Water and Antarctic Surface Water (Moffat and Meredith, 2018). Proximal to the ice front, there is a subtle shift in  $\theta$ - $S$  space to fresher water, tightly correlating with the glacial melt Gade line. Along the mixing line for these stations, beam transmission signals as low as 40% are observed in water at depths of 50–150 m. The grounding line of the Sheldon Glacier on the western side of the cove is 200–220 deep, and typically 105 m

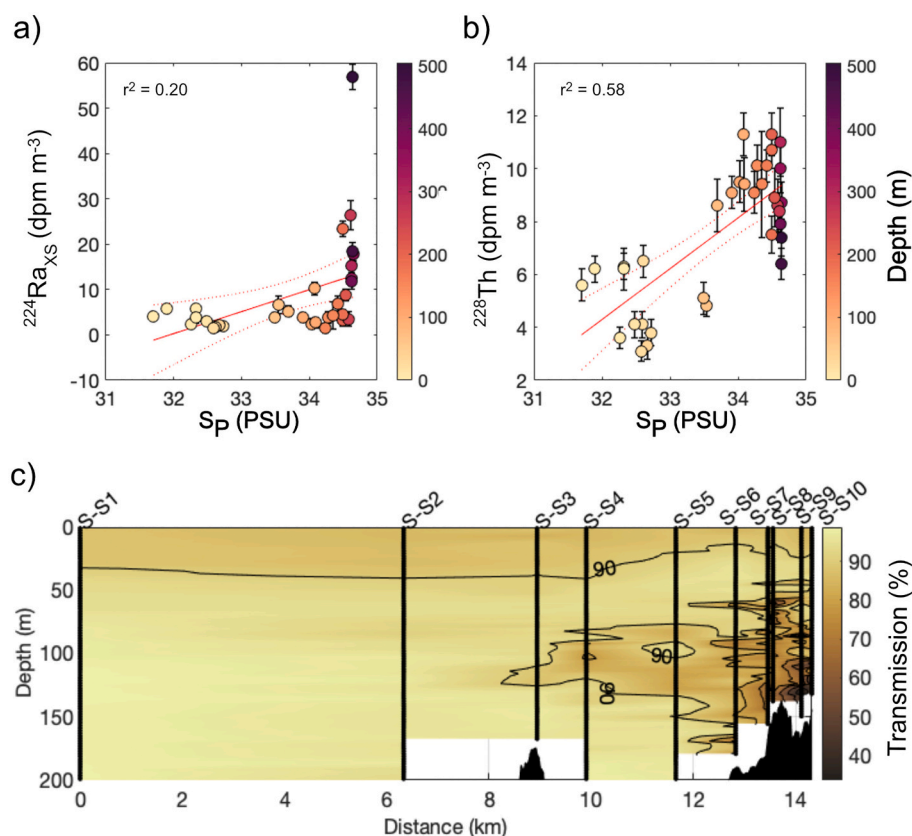


**Fig. 10.** Short-lived radiogenic isotope activities plotted with salinity, shaded with depth for a)  $^{224}\text{Ra}_{\text{XS}}$  and b)  $^{228}\text{Th}$  and associated errors at Sheldon Cove. The red line and dotted red lines indicate the linear regression and 95% confidence intervals, respectively;  $r$ -squared values are shown on each subplot c) Transmission data across Sheldon Cove in the top 200 m. (For interpretation of the references to colour in this figure legend, the reader is referred to the web version of this article.)

**Table 2**

Parameters for vertical macronutrient flux calculations, based on the change in  $^{224}\text{Ra}_{\text{XS}}$  with vertical distance from the benthic boundary, and eddy diffusion.

	Unit	S-S2	S-S4	S-S6
Profile upper depth	<i>m</i>	150	35	20
Profile lower depth	<i>m</i>	470	269	90
$^{224}\text{Ra}_{\text{XS}}$ gradient	$\text{dpm m}^{-3} \text{m}^{-1}$	0.068	0.103	0.125
$K_h$	$\text{m}^2 \text{s}^{-1}$	$9.6 \times 10^{-3}$	$8.8 \times 10^{-2}$	$2.8 \times 10^{-3}$
$^{224}\text{Ra}_{\text{XS}}$ flux	$\text{dpm m}^{-2} \text{s}^{-1}$	$1.0 \times 10^{-3}$	$9.0 \times 10^{-3}$	$3.0 \times 10^{-4}$
$\text{Si}(\text{OH})_4$ flux	$\text{mmol m}^{-2} \text{d}^{-1}$	0.038	0.12	0.096
$\text{NO}_3^-$ flux	$\text{mmol m}^{-2} \text{d}^{-1}$	–	–	$5.8 \times 10^{-2}$
$\text{PO}_4^{3-}$ flux	$\text{mmol m}^{-2} \text{d}^{-1}$	–	–	$3.9 \times 10^{-3}$

deep along the northern edge of the cove (varying between 70 m and 120 m). Near sample S–S9, the grounding line is 105–110 m deep. Across these depths, our findings would indicate that glacial melt drives vigorous mixing of suspended material into the water column. Combining the vertical fluxes of radium, high  $^{228}\text{Th}$  and transmission signals and resolved vertical macronutrient fluxes, we infer that glacial melt rises buoyantly upwards, bringing lithogenic material and macronutrient-rich deep water surfacewards.

Cape et al. (2019b) provided the first evidence of nutrient entrainment as an important physical process for marine-terminating glaciers at the WAP in the upwelling and export of macronutrients to the shelf, supplying primary productivity beyond the bay. Studies of Greenlandic marine-terminating fjords indicated buoyant meltwater drives vertical transport of ambient waters up to 10–30 times greater in volume than the initial meltwater discharge (Beaird et al., 2015; Bendtsen et al.,

2015; Beaird et al., 2018), bringing nutrient-rich deep waters upwards, supplying the photic zone (Kanna et al., 2018; Meire et al., 2017; Cape et al., 2019a). Arctic-based studies estimate total fluxes of nitrate on the order of  $14\text{--}400 \times 10^4 \text{ mol d}^{-1}$  within glacial fjords (Halbach et al., 2019; Kanna et al., 2018; Meire et al., 2017). These calculations used estimated volumetric meltwater discharge and varying entrainment factors ( $3\text{--}14 \times$  volumetric discharge) across the total area of the fjord. Using the nitrate flux of  $0.058 \text{ mmol m}^{-2} \text{d}^{-1}$  calculated at S–S6 and multiplying it by the profile depth (70 m), the estimated cove width (2500 m) and distance from S–S6 to the ice edge (2000 m), gives a total flux of  $20 \times 10^4 \text{ mol d}^{-1}$ , which is comparable with the cited estimates above. This derivation assumes that eddy diffusion is constant over the width of the cove along the depth profile, and that melting occurs across the full width of the cove, but also assumes no entrainment of mCDW past S–S6. These assumptions could result in over- and underestimates in our calculation, respectively, to the same order of magnitude ( $\sim 1 \text{ km}$ ), so we suggest our estimate is reasonable.

### 5.6. Implications of continued glacial retreat

Our results indicate that buoyant glacial meltwater at Sheldon Cove drives vertical entrainment of nutrient rich mCDW to surface waters, with additional inputs from the mixing of  $\text{Si}(\text{OH})_4$ -rich porewaters over the sill. Arctic fjords fed by large marine-terminating glaciers show a strong link between nutrient entrainment driven by subglacial discharge and elevated productivity (Meire et al., 2017; Kanna et al., 2018). Fluorescence data presented in Supplementary Fig. S6 shows higher fluorescence at Sheldon Cove than Marian Cove, and previous studies have shown high total chlorophyll-*a* levels of up to  $25 \mu\text{g L}^{-1}$  during the summer at S–S1 (RaTS sampling station) (Henley et al., 2017). Marian Cove has also experienced summer blooms: Kim et al. (2021) found total



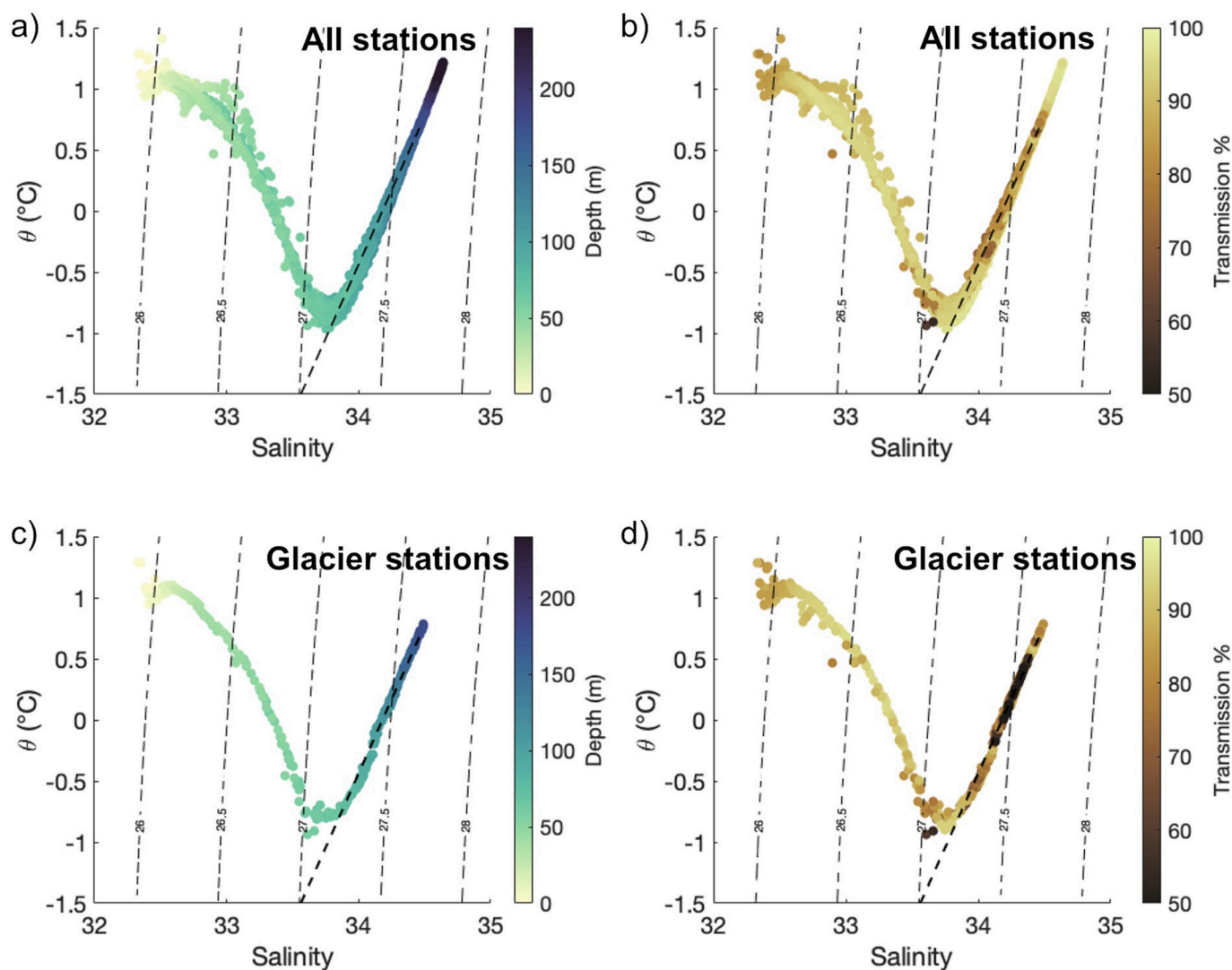


**Fig. 11.** Potential Temperature – salinity plots for Sheldon Cove CTD casts, with potential density contours, plotted by a) depth and b) transmission for all stations, and c) depth and d) transmission, for stations S–S6 to S–S10. The black dotted line represents the Gade line (Gade, 1979), a mixing line for seawater with glacial melt.

chlorophyll-*a* levels at Marian Cove of up to  $19.5 \mu\text{g L}^{-1}$  during January 2019. However, the high turbidity associated with sediment-laden meltwater inputs and strong wind forcing have been used to previously explain the typically low phytoplankton biomass in the region, despite replete nutrient levels (Schloss et al., 2012). We suggest that the lower productivity at Marian Cove compared to Sheldon Cove is likely due to unfavourable physical conditions at Marian Cove, subglacial nutrient entrainment at Sheldon Cove, or both. A regional shift towards more land-terminating glaciers would impact both these processes. Future work should analyse the impact of high suspended material loads from meltwaters upon primary productivity, to help elucidate the future drivers of productivity and carbon uptake with continued acceleration of glacial retreat both sub-glacially and over land.

## 6. Conclusions

The rising prevalence of land-terminating glaciers at the WAP is of concern regarding changes to phytoplankton community composition and primary production, both of which influence productivity throughout the food web and the efficiency of ocean carbon uptake in the region. Our findings highlight the importance of the interaction between glacial melt and sediments in glacial bay biogeochemistry

along the West Antarctic Peninsula. We present a high-resolution short-lived radium and thorium isotope dataset which provides a spatial and temporal analysis of the impact of both land- and marine-terminating glaciers upon water column sediment and nutrient cycling. Using radium-derived eddy diffusion fluxes, the estimated nitrate entrainment in the order of  $10^5 \text{ mol d}^{-1}$  suggests glacial melt entrainment of mCDW could be an important process along the WAP, and changes in meltwater input rates should be recognised as key drivers for macronutrient distributions proximal to the glacier edge.

These findings highlight the need to further study regions fed by newly land-terminating glaciers, extracting meltwater signals at high resolution to capture important glacier-ocean interactions. Methods to ensure high-resolution vertical sampling include sample collection by hand using small boats, or deploying Autonomous Surface Vehicles and Autonomous Underwater Vehicles with fitted sensors, which have increased potential vertical and horizontal resolution for measurements, and spatial and temporal coverage in remote locations (Whitt et al., 2020).

Future work should target the direct impact of meltwater fluxes upon primary productivity and community composition along the West Antarctic Peninsula, to advance our understanding of the local limitations on productivity and the potential for nutrient export offshore. Tracing

the fate of macronutrients beyond the coastal zone could help inform predictive studies on the impact of glacial retreat upon primary productivity across the Southern Ocean as a whole.

### Declaration of Competing Interest

None.

### Data availability

For the CTD data: [www.bodc.ac.uk/data/published\\_data\\_library/catalogue/10.5285/d9633a6c-d27e-30b4-e053-6c86abc07104](http://www.bodc.ac.uk/data/published_data_library/catalogue/10.5285/d9633a6c-d27e-30b4-e053-6c86abc07104) (DOI: 10.5285/d9633a6c-d27e-30b4-e053-6c86abc07104).

For the multibeam bathymetry data: The multibeam bathymetry data are available at 5-m gridded resolution at <https://data.bas.ac.uk/full-record.php?id=GB/NERC/BAS/PDC/01511>. The radium data is provided in the Supplementary Materials.

### Acknowledgements

We gratefully acknowledge the officers, crew, and scientists aboard the JR19002 cruise for all the assistance and support with data collection. Particularly, thanks to Tobias Ehmen, Carmen Falagan-Rodriguez, Marina Costa, Christopher Bull, Seth Thomas, and Thomas Owen as Multibeam Echosounder and CTD operators, Aisling Smith for lab support, and Alice Fremand for data management support.

The study was carried out as part of the Radium in Changing Environments: A Novel Tracer of Iron Fluxes at Ocean Margins (RaCE:TraX) grant (NE/P017630/1). Additional funding for RJ comes from the National Environmental Research Council INSPIRE Doctoral Training Partnership (NE/S007210/1) and Harry Elderfield Memorial Scholarship.

### Appendix A. Supplementary data

Supplementary data to this article can be found online at <https://doi.org/10.1016/j.marchem.2023.104230>.

### References

- Annett, A., Henley, S.F., Van Beek, P., Ganeshram, R., Venables, H.J., Meredith, M.P., Geibert, W., 2013. Use of radium isotopes to estimate mixing rates and trace sediment inputs to surface waters in northern Marguerite Bay (Antarctic Peninsula). *Antarct. Sci.* 25, 445–456.
- Annett, A.L., Fitzsimmons, J.N., Séguret, M.J., Lagerström, M., Meredith, M.P., Schofield, O., Sherrill, R.M., 2017. Controls on dissolved and particulate iron distributions in surface waters of the Western Antarctic Peninsula shelf. *Mar. Chem.* 196, 81–97.
- Beard, N., Straneo, F., Jenkins, W., 2015. Spreading of Greenland meltwaters in the ocean revealed by noble gases. *Geophys. Res. Lett.* 42, 7705–7713.
- Beard, N.L., Straneo, F., Jenkins, W., 2018. Export of strongly diluted Greenland meltwater from a major glacial fjord. *Geophys. Res. Lett.* 45, 4163–4170.
- Becker, S., Aoyama, M., Woodward, E.M.S., Bakker, K., Coverly, S., Mahaffey, C., Tanhua, T., 2020. GO-SHIP repeat hydrography nutrient manual: the precise and accurate determination of dissolved inorganic nutrients in seawater, using continuous flow analysis methods. *Front. Mar. Sci.* 7, 908.
- Bendtsen, J., Mortensen, J., Rysgaard, S., 2015. Modelling subglacial discharge and its influence on ocean heat transport in Arctic fjords. *Ocean Dyn.* 65, 1535–1546.
- Bown, J., Van Haren, H., Meredith, M.P., Venables, H.J., Laan, P., Brearley, J.A., De Baar, H.J., 2018. Evidences of strong sources of DFe and DMn in Ryder Bay, Western Antarctic Peninsula. *Philos. Trans. R. Soc. A Math. Phys. Eng. Sci.* 376, 20170172.
- Broecker, W., Kaufman, A., Trier, R., 1973. The residence time of thorium in surface sea water and its implications regarding the rate of reactive pollutants. *Earth Planet. Sci. Lett.* 20, 35–44.
- Brown, M.T., Lippiatt, S.M., Bruland, K.W., 2010. Dissolved aluminum, particulate aluminum, and silicic acid in northern Gulf of Alaska coastal waters: glacial/riverine inputs and extreme reactivity. *Mar. Chem.* 122, 160–175.
- Cape, M.R., Straneo, F., Beard, N., Bundy, R.M., Charette, M.A., 2019a. Nutrient release to oceans from buoyancy-driven upwelling at Greenland tidewater glaciers. *Nat. Geosci.* 12, 34–39.
- Cape, M.R., Vernet, M., Pettit, E.C., Wellner, J., Truffer, M., Akie, G., Domack, E., Leventer, A., Smith, C.R., Huber, B.A., 2019b. Circumpolar deep water impacts glacial meltwater export and coastal biogeochemical cycling along the West Antarctic Peninsula. *Front. Mar. Sci.* 6.
- Cassarino, L., Hendry, K.R., Henley, S.F., Macdonald, E., Arndt, S., Freitas, F.S., Pike, J., Firing, Y.L., 2020. Sedimentary nutrient supply in productive hotspots off the West Antarctic Peninsula revealed by silicon isotopes. *Glob. Biogeochem. Cycles* 34 (12).
- Cochran, J., Masqué, P., 2003. Short-lived U/Th series radionuclides in the ocean: tracers for scavenging rates, export fluxes and particle dynamics. *Rev. Mineral. Geochem.* 52, 461–492.
- Cook, A.J., Holland, P., Meredith, M., Murray, T., Luckman, A., Vaughan, D.G., 2016. Ocean forcing of glacier retreat in the western Antarctic Peninsula. *Science* 353, 283–286.
- Corbett, D.R., Crenshaw, J., Null, K., Peterson, R.N., Peterson, L.E., Lyons, W.B., 2017. Nearshore mixing and nutrient delivery along the western Antarctic Peninsula. *Antarct. Sci.* 29, 397–409.
- Diego-Feliu, M., Rodellas, V., Alorda-Kleinglass, A., Tamborski, J., Van Beek, P., Heins, L., Bruach, J., Arnold, R., Garcia-Orellana, J., 2020. Guidelines and limits for the quantification of Ra isotopes and related radionuclides with the radium delayed coincidence counter (RaDeCC). *J. Geophys. Res. Oceans* 125 e2019JC015544.
- Dierssen, H.M., Smith, R.C., Vernet, M., 2002. Glacial meltwater dynamics in coastal waters west of the Antarctic peninsula. *Proc. Natl. Acad. Sci.* 99, 1790–1795.
- Dotto, T.S., Kerr, R., Mata, M.M., Garcia, C.A., 2016. Multidecadal freshening and lightening in the deep waters of the Bransfield Strait, Antarctica. *J. Geophys. Res. Oceans* 121, 3741–3756.
- Dulaiova, H., et al., 2009. Shelf-derived iron inputs drive biological productivity in the southern Drake Passage. *Glob. Biogeochem. Cycles* 23.
- Epstein, S., Mayeda, T., 1953. Variation of O18 content of waters from natural sources. *Geochim. Cosmochim. Acta* 4, 213–224.
- Falk, U., Gieseke, H., Kotzur, F., Braun, M., 2016. Monitoring snow and ice surfaces on King George Island, Antarctic Peninsula, with high-resolution TerraSAR-X time series. *Antarct. Sci.* 28, 135–149.
- Falk, U., López, D.A., Silva-Busso, A., 2018. Multi-year analysis of distributed glacier mass balance modelling and equilibrium line altitude on King George Island, Antarctic Peninsula. *Cryosphere* 12, 1211–1232.
- Ferreira, A., Costa, R.R., Dotto, T.S., Kerr, R., Tavano, V.M., Brito, A.C., Brotas, V., Secchi, E.R., Mendes, C.R., 2020. Changes in phytoplankton communities along the northern Antarctic Peninsula: causes, impacts and research priorities. *Front. Mar. Sci.* 7, 576254.
- Gade, H.G., 1979. Melting of ice in sea water: a primitive model with application to the Antarctic ice shelf and icebergs. *J. Phys. Oceanogr.* 9, 189–198.
- Garcia-Solsona, E., Garcia-Orellana, J., Masqué, P., Dulaiova, H., 2008. Uncertainties associated with 223Ra and 224Ra measurements in water via a delayed coincidence counter (RaDeCC). *Mar. Chem.* 109, 198–219.
- Gerringa, L.J., Alderkamp, A.-C., Laan, P., Thuroczy, C.-E., De Baar, H.J., Mills, M.M., Van Dijken, G.L., Van Haren, H., Arrigo, K.R., 2012. Iron from melting glaciers fuels the phytoplankton blooms in Amundsen Sea (Southern Ocean): Iron biogeochemistry. *Deep-Sea Res. II Top. Stud. Oceanogr.* 71, 16–31.
- Halbach, L., Assmy, P., Vihtakari, M., Hop, H., Duarte, P., Wold, A., Kauko, H.M., Kristiansen, S., Everett, A., Myhre, P.I., 2019. Tidewater glaciers and bedrock characteristics control the phytoplankton growth environment in an Arctic fjord. *Front. Mar. Sci.* 6, 254.
- Hawkins, J.R., Benning, L.G., Raiswell, R., Kaulich, B., Araki, T., Abyaneh, M., Stockdale, A., Koch-Müller, M., Wadhams, J.L., Tranter, M., 2018. Biolabile ferrous iron bearing nanoparticles in glacial sediments. *Earth Planet. Sci. Lett.* 493, 92–101.
- Hendry, K.R., Huvenne, V.A., Robinson, L.F., Annett, A., Badger, M., Jacobel, A.W., NG, H.C., Opher, J., Pickering, R.A., Taylor, M.L., 2019. The biogeochemical impact of glacial meltwater from Southwest Greenland. *Prog. Oceanogr.* 176, 102126.
- Henley, S.F., Tuerena, R.E., Annett, A.L., Fallick, A.E., Meredith, M.P., Venables, H.J., Clarke, A., Ganeshram, R.S., 2017. Macronutrient supply, uptake and recycling in the coastal ocean of the west Antarctic Peninsula. *Deep-Sea Res. II Top. Stud. Oceanogr.* 139, 58–76.
- Henley, S.F., Jones, E.M., Venables, H.J., Meredith, M.P., Firing, Y.L., Dittrich, R., Heiser, S., Stefels, J., Dougan, J., 2018. Macronutrient and carbon supply, uptake and cycling across the Antarctic Peninsula shelf during summer. *Philos. Trans. R. Soc. A Math. Phys. Eng. Sci.* 376, 20170168.
- Hodson, A., Mumford, P., Kohler, J., Wynn, P.M., 2005. The High Arctic glacial ecosystem: new insights from nutrient budgets. *Biogeochemistry* 72, 233–256.
- Hodson, A., Nowak, A., Sabacka, M., Jungblut, A., Navarro, F., Pearce, D., Ávila-Jiménez, M.L., Convey, P., Vieira, G., 2017. Climatically sensitive transfer of iron to maritime Antarctic ecosystems by surface runoff. *Nat. Commun.* 8, 1–7.
- Hoffmann, R., Al-Handal, A.Y., Wulff, A., Deregis, D., Zacher, K., Quartino, M.L., Wenzhöfer, F., Braeckman, U., 2019. Implications of glacial melt-related processes on the potential primary production of a microphytobenthic community in Potter Cove (Antarctica). *Front. Mar. Sci.* 6, 655.
- Holding, J.M., Markager, S., Juul-Pedersen, T., Paulsen, M.L., Møller, E.F., Meire, L., Sejr, M.K., 2019. Seasonal and spatial patterns of primary production in a high-latitude fjord affected by Greenland Ice Sheet run-off. *Biogeosciences* 16 (19), 3777–3792.
- Kanna, N., Sugiyama, S., Ohashi, Y., Sakakibara, D., Fukamachi, Y., Nomura, D., 2018. Upwelling of macronutrients and dissolved inorganic carbon by a subglacial freshwater driven plume in Bowdoin Fjord, northwestern Greenland. *J. Geophys. Res. Biogeosci.* 123, 1666–1682.
- Kim, B.K., Jeon, M., Joo, H.M., Kim, T.W., Park, S.J., Park, J., Ha, S.Y., 2021. Impact of Freshwater Discharge on the Carbon Uptake Rate of Phytoplankton During Summer (January–February 2019) in Marian Cove, King George Island, Antarctica. *Front. Mar. Sci.* 8, 725173.
- Lippiatt, S.M., Lohan, M.C., Bruland, K.W., 2010. The distribution of reactive iron in northern Gulf of Alaska coastal waters. *Mar. Chem.* 121, 187–199.

- Maiti, K., Charette, M.A., Buesseler, K.O., Zhou, K., Henderson, P., Moore, W.S., Morris, P., Kipp, L., 2015. Determination of particulate and dissolved <sup>228</sup>Th in seawater using a delayed coincidence counter. *Mar. Chem.* 177, 196–202.
- Massom, R.A., Scambos, T.A., Bennetts, L.G., Reid, P., Squire, V.A., Stammerjohn, S.E., 2018. Antarctic ice shelf disintegration triggered by sea ice loss and ocean swell. *Nature* 558, 383–389.
- Meire, L., Meire, P., Struyf, E., Krawczyk, D., Arendt, K., Yde, J., Juul Pedersen, T., Hopwood, M.J., Rysgaard, S., Meysman, F., 2016. High export of dissolved silica from the Greenland Ice Sheet. *Geophys. Res. Lett.* 43, 9173–9182.
- Meire, L., Mortensen, J., Meire, P., Juul-Pedersen, T., Sej, M.K., Rysgaard, S., Nygaard, R., Huybrechts, P., Meysman, F.J., 2017. Marine-terminating glaciers sustain high productivity in Greenland fjords. *Glob. Chang. Biol.* 23, 5344–5357.
- Meredith, M.P., Brandon, M.A., Wallace, M.I., Clarke, A., Leng, M.J., Renfrew, I.A., Van Lipzig, N.P., King, J.C., 2008. Variability in the freshwater balance of northern Marguerite Bay, Antarctic Peninsula: results from  $\delta^{18}O$ . *Deep-Sea Res. II Top. Stud. Oceanogr.* 55, 309–322.
- Meredith, M.P., Wallace, M.I., Stammerjohn, S.E., Renfrew, I.A., Clarke, A., Venables, H. J., Shoosmith, D.R., Souster, T., Leng, M.J., 2010. Changes in the freshwater composition of the upper ocean west of the Antarctic Peninsula during the first decade of the 21st century. *Prog. Oceanogr.* 87, 127–143.
- Meredith, M.P., Stammerjohn, S.E., Venables, H.J., Ducklow, H.W., Martinson, D.G., Iannuzzi, R.A., Leng, M.J., Van Wessem, J.M., Reijmer, C.H., Barrand, N.E., 2017. Changing distributions of sea ice melt and meteoric water west of the Antarctic Peninsula. *Deep-Sea Res. II Top. Stud. Oceanogr.* 139, 40–57.
- Meredith, M.P., Falk, U., Bers, A.V., Mackensen, A., Schloss, I.R., Ruiz Barlett, E., Jerosch, K., Silva Busso, A., Abele, D., 2018. Anatomy of a glacial meltwater discharge event in an Antarctic cove. *Philos. Trans. R. Soc. A Math. Phys. Eng. Sci.* 376, 20170163.
- Moffat, C., Meredith, M., 2018. Shelf–ocean exchange and hydrography west of the Antarctic Peninsula: a review. *Philos. Trans. R. Soc. A Math. Phys. Eng. Sci.* 376, 20170164.
- Moline, M.A., Claustre, H., Frazer, T.K., Schofield, O., Vernet, M., 2004. Alteration of the food web along the Antarctic peninsula in response to a regional warming trend. *Glob. Chang. Biol.* 10, 1973–1980.
- Moore, W.S., 2000. Determining coastal mixing rates using radium isotopes. *Cont. Shelf Res.* 20, 1993–2007.
- Moore, W.S., 2008. Fifteen years experience in measuring <sup>224</sup>Ra and <sup>223</sup>Ra by delayed-coincidence counting. *Mar. Chem.* 109, 188–197.
- Ng, H.C., Cassarino, L., Pickering, R.A., Woodward, E.M.S., Hammond, S.J., Hendry, K. R., 2020. Sediment efflux of silicon on the Greenland margin and implications for the marine silicon cycle. *Earth Planet. Sci. Lett.* 529, 115877.
- Null, K.A., Corbett, D.R., Crenshaw, J., Peterson, R.N., Peterson, L.E., Lyons, W.B., 2019. Groundwater discharge to the western Antarctic coastal ocean. *Polar. Res.* 38.
- Östlund, H.G., Hut, G., 1984. Arctic Ocean water mass balance from isotope data. *J. Geophys. Res. Oceans* 89, 6373–6381.
- Pan, B.J., Vernet, M., Manck, L., Forsch, K., Ekern, L., Mascioni, M., Barbeau, K.A., Almandoz, G.O., Orona, A.J., 2020. Environmental drivers of phytoplankton taxonomic composition in an Antarctic fjord. *Prog. Oceanogr.* 183, 102295.
- Pedulli, M., Bisagni, J.J., Ducklow, H.W., Beardsley, R., Pilskaln, C., 2014. Estimates of potential new production (PNP) for the waters off the western Antarctic Peninsula (WAP) region. *Cont. Shelf Res.* 84, 54–69.
- Rignot, E., Casassa, G., Gogineni, P., Krabill, W., Rivera, A., Thomas, R., 2004. Accelerated ice discharge from the Antarctic Peninsula following the collapse of Larsen B ice shelf. *Geophys. Res. Lett.* 31.
- Sahade, R., Lagger, C., Torre, L., Momo, F., Monien, P., Schloss, I., Barnes, D.K., Servetto, N., Tarantelli, S., Tatián, M., 2015. Climate change and glacier retreat drive shifts in an Antarctic benthic ecosystem. *Sci. Adv.* 1, e1500050.
- Schloss, I., Klöser, H., Ferreyra, G., Mercuri, G., Pinola, E., 1997. Factors governing phytoplankton and particulate matter variation in Potter Cove, King George island, Antarctica. *Antarctic Commun.* 135–141.
- Schloss, I.R., Abele, D., Moreau, S., Demers, S., Bers, A.V., González, O., Ferreyra, G.A., 2012. Response of phytoplankton dynamics to 19-year (1991–2009) climate trends in Potter Cove (Antarctica). *J. Mar. Syst.* 92, 53–66.
- Schloss, I.R., Wasilowska, A., Dumont, D., Almandoz, G.O., Hernando, M.P., Michaud-Tremblay, C.A., Ferreyra, G.A., 2014. On the phytoplankton bloom in coastal waters of southern King George Island (Antarctica) in January 2010: an exceptional feature? *Limnol. Oceanogr.* 59 (1), 195–210.
- Schlosser, P., Bayer, R., Foldvik, A., Gammelsrød, T., Rohardt, G., Münnich, K.O., 1990. Oxygen 18 and helium as tracers of ice shelf water and water/ice interaction in the Weddell Sea. *J. Geophys. Res. Oceans* 95, 3253–3263.
- Schmidtke, S., Heywood, K.J., Thompson, A.F., Aoki, S., 2014. Multidecadal warming of Antarctic waters. *Science* 346, 1227–1231.
- Selzer, S., Annett, A.L., Homoky, W.B., 2021. RaDeCC reader: fast, accurate and automated data processing for radium delayed coincidence counting systems. *Comput. Geosci.* 149, 104699.
- Stammerjohn, S., Maksym, T., Massom, R., Lowry, K., Arrigo, K., Yuan, X., Raphael, M., Randall-Goodwin, E., Sherrell, R., Yager, P., 2015. Seasonal sea ice changes in the Amundsen Sea, Antarctica, over the period of 1979–2014. *Seasonal sea ice changes in the Amundsen Sea. Elementa* 3.
- Sun, Y., Torgersen, T., 1998. The effects of water content and Mn-fiber surface conditions on <sup>224</sup>Ra measurement by <sup>220</sup>Rn emanation. *Mar. Chem.* 62, 299–306.
- Turner, J., Hosking, J.S., Bracegirdle, T.J., Marshall, G.J., Phillips, T., 2015. Recent changes in Antarctic Sea ice. *Philos. Trans. R. Soc. A Math. Phys. Eng. Sci.* 373, 20140163.
- Venables, H.J., Meredith, M.P., Brearley, J.A., 2017. Modification of deep waters in Marguerite Bay, western Antarctic Peninsula, caused by topographic overflows. *Deep-Sea Res. II Top. Stud. Oceanogr.* 139, 9–17.
- Weiss, R., Östlund, H., Craig, H., 1979. Geochemical studies of the Weddell Sea. *Deep Sea research part A. Oceanogr. Res. Pap.* 26, 1093–1120.
- Whitt, C., Pearlman, J., Polagye, B., Caimi, F., Muller-Karger, F., Copping, A., Spence, H., Madhusudhana, S., Kirkwood, W., Grosjean, L., 2020. Future vision for autonomous ocean observations. *Front. Mar. Sci.* 697.
- Woodward, E., Rees, A., 2001. Nutrient distributions in an anticyclonic eddy in the Northeast Atlantic Ocean, with reference to nanomolar ammonium concentrations. *Deep-Sea Res. II Top. Stud. Oceanogr.* 48, 775–793.